

## Sensitivity of the Northern Humboldt Current System nearshore modeled circulation to initial and boundary conditions

Vincent Echevin,<sup>1</sup> Francois Colas,<sup>2</sup> Alexis Chaigneau,<sup>1,3</sup> and Pierrick Penven<sup>4</sup>

Received 29 September 2010; revised 23 December 2010; accepted 17 March 2011; published 2 July 2011.

[1] The influence of the eastern Pacific equatorial circulation on the dynamics of the Northern Humboldt Current System is studied using an eddy-resolving regional circulation model forced by boundary conditions from three distinct ocean general circulation models. The seasonal variability of the modeled nearshore circulation and the mesoscale activity are contrasted in order to evaluate the role of the density forcing. The seasonal variability of the surface and subsurface alongshore currents strongly depends on the amplitude and timing of the seasonal eastward propagating equatorial waves. The equatorward flow and upwelling intensity are also impacted by nonlinear processes, such as the seasonal generation of nearshore mesoscale eddies, which create alongshore pressure gradients modulating the surface current. Boundary conditions affect differently the intensity and phase of the eddy kinetic energy, as baroclinic instability is triggered by coastal waves during austral summer and fall, whereas it is sustained by the wind-driven upwelling during austral winter.

**Citation:** Echevin, V., F. Colas, A. Chaigneau, and P. Penven (2011), Sensitivity of the Northern Humboldt Current System nearshore modeled circulation to initial and boundary conditions, *J. Geophys. Res.*, 116, C07002, doi:10.1029/2010JC006684.

### 1. Introduction

[2] The Northern Humboldt Current System (NHCS) is a site of permanent wind-driven coastal upwelling, which is associated with an intense biological activity and a rich ecosystem [Chavez *et al.*, 2008]. To compensate the wind-driven offshore Ekman transport, the nearshore pycnocline is lifted upward leading to a cross-shore density gradient which in turn drives the equatorward Peru Coastal Current (PCC, Figure 1a) by geostrophic adjustment. The NHCS is also composed of two poleward currents, namely the subsurface Peru-Chile Undercurrent (PCUC) [Silva and Neshyba, 1979] (Figure 1a) and the offshore surface Peru-Chile Countercurrent (PCCC) [Strub *et al.*, 1995, 1998; Penven *et al.*, 2005, hereinafter PEN05]. The PCUC, which transports nutrient-rich waters to be upwelled nearshore, is partly connected to the subsurface Equatorial Undercurrent (EUC, Figure 1a), which flows eastward at around 50–100 m depth along the equator [Kessler, 2006]. When reaching the Galapagos Islands near 92°W, the EUC splits into several branches, which flow around the Archipelago and feed the PCUC [Lukas, 1986; Kessler, 2006]. The PCUC may also be related to the zonal eastward flowing subsurface counter-currents (SSCCs) centered near 4°S and 8°S at 100–150 m depth, as evidenced by observations [Kessler, 2006] and in

a recent modeling study [Montes *et al.*, 2010, hereinafter MON10]. For a complete description of the current system, the reader is referred to Figure 1 of MON10.

[3] Previous modeling work based on the Regional Ocean Modeling System (ROMS) model [Shchepetkin and McWilliams, 2005] has provided insight on the NHCS dynamical processes at seasonal and interannual (ENSO) time scales [PEN05; MON10; Colas *et al.*, 2008], and has been used as a background for the study of biological processes [Lett *et al.*, 2007; Brochier *et al.*, 2008]. In these studies as in most regional modeling experiments, the methodology to drive the circulation through the open boundary forcing is generally the following: dynamical (velocities and sea level) and hydrological fields (temperature, salinity) from an ocean general circulation model (OGCM) or a climatological Atlas are interpolated onto the regional model grid and along its open boundaries. During the course of the model integration, an open boundary condition (OBC) numerical scheme is used to infer the boundary values most consistent with both the external forcing and the regional model's dynamics [Marchesiello *et al.*, 2001]. Consequently, different sets of initial and time-variable boundary conditions result in different model equilibrium solutions.

[4] Various dynamical processes are driven by the large-scale initial and boundary conditions in the NHCS. First, the initial density field influences the vertical structure and intensity of the coastal currents. For instance, the intensity and depth of the offshore pycnocline constrain the vertical displacement of the near-coastal pycnocline during coastal upwelling, and thus impact the surface cross-shore density gradient which forces the PCC through geostrophy. In the near-coastal region, the density field is also modulated

<sup>1</sup>LOCEAN/IRD/IPSL/UPMC, Paris, France.

<sup>2</sup>CESR, IGPP, UCLA, Los Angeles, California, USA.

<sup>3</sup>IMARPE, Callao, Peru.

<sup>4</sup>UMR 5563, LPO/IRD/UBO, Plouzané, France.

by the mass inflow from the model's lateral boundaries. Offshore water masses are transported by off-equatorial SSCs near 4°S and 8°S and by the PCUC before being upwelled in the near-coastal region [MON10]. This can induce alongshore pressure gradients which influence the NHCS momentum balance. Second, the offshore equatorial circulation impacts the NHCS through the eastward propagation of equatorial Kelvin waves (EKWs). When reaching the South American coasts, EKWs trigger coastally trapped waves (CTWs) [Clarke, 1983] which modify the coastal currents by uplifting or deepening the nearshore pycnocline during their alongshore poleward propagation.

[5] In the present study, we assess the dependence of the NHCS coastal and mesoscale circulation to the regional model initial and boundary conditions. Three equilibrium solutions of the ROMS model were forced by three different OGCM initial and boundary conditions. The OGCMs were selected as to provide different stratification and equatorial circulation for each simulation. We particularly focus on the spatiotemporal variations of the PCC, PCUC, and nearshore mesoscale activity which is modulated by the horizontal and vertical kinematical shears in the coastal region. In section 2 we present the data and methods, and in section 3 the results of the simulations. A discussion is presented in section 4, and conclusions are summarized in section 5.

## 2. Data and Methods

### 2.1. The ROMS Model

[6] The ROMS-AGRIF model (<http://roms.mpl.ird.fr/>) used in this study solves the primitive equations in an Earth centered rotating environment, based on the Boussinesq approximation and hydrostatic vertical momentum balance. It is discretized in terrain-following vertical coordinates. The third-order, upstream-biased advection scheme implemented in ROMS allows the generation of steep gradients, enhancing the effective resolution of the solution for a given grid size [Shchepetkin and McWilliams, 1998]. Explicit lateral viscosity is null everywhere in the model domain, except in sponge layers near the open boundaries where it increases smoothly on a few grid points. A nonlocal, K profile planetary boundary layer scheme [Large et al., 1994] parameterizes the subgrid-scale vertical mixing processes. For more details on the model parameterizations, the reader is referred to Shchepetkin and McWilliams [2009]. We used the same model configuration developed by PEN05 and used by MON10. The horizontal grid is isotropic ( $\Delta x = \Delta y = 1/9^\circ$ , corresponding to  $\sim 13$  km in the study region) and contains  $192 \times 240$  points that span the region between 4°N and 22°S and from 70°W to 90°W (Figure 1a). The western boundary intersects the Galapagos Islands at 0.6°S.

[7] The bottom topography derived from the ETOPO2 database [Smith and Sandwell, 1997] has been smoothed in order to reduce potential error in the horizontal pressure gradient. The model possesses 32 stretched vertical sigma levels to obtain a vertical resolution ranging from 0.3 m to 6.25 m for the surface layer and from 0.3 m to 1086 m for the bottom layer.

### 2.2. Boundary Conditions

[8] The three open boundaries (northern, western and southern) of the ROMS model are forced by temperature,

salinity and velocity fields obtained from an OGCM using OBC parameterizations described by Marchesiello et al. [2001]. We used outputs of three distinct OGCMs in climatological mode. The initial state corresponds to the mean temperature and salinity conditions in January, and monthly climatologies were computed to provide a set of monthly OBCs. The OGCMs characteristics are listed below:

[9] 1. The OCCAM [Saunders et al., 1999] OGCM at  $1/4^\circ$  resolution was forced repeatedly by a climatology of monthly winds constructed from the years 1986–1988 of the ECMWF atmospheric model. As with PEN05 and MON10, the monthly climatology was constructed from a 10 year period of OCCAM outputs.

[10] 2. The SODA [Carton and Giese, 2008] OGCM at  $1/2^\circ$  resolution was forced by interannual ERA-40 surface fluxes [Uppala et al., 2005], and constrained by data assimilation of in situ and altimetric satellite data, which produced the SODA1.4.2 reanalysis. The monthly climatology was constructed from the 1980–2000 period, as with MON10.

[11] 3. The ORCA [Madec et al., 1998] OGCM at  $1/2^\circ$  resolution was constructed from an 8 year simulation forced by weekly ERS winds and NCEP heat fluxes [Lengaigne et al., 2002; C. Eth  , personal communication, 2005]. The monthly climatology was constructed from the 1992–2000 period.

[12] The three OGCM outputs were interpolated onto the ROMS model grid to construct initial state and boundary forcing using the ROMSTOOLS package [Penven et al., 2008]. The boundary condition is a mixed radiative-relaxation parameterization [Marchesiello et al., 2001]. OBC variables are restored toward climatological values with a time scale of 1 day (180 days) in case of inflow (outflow). The so-called Flather boundary condition is imposed on the 2D momentum equations and an Orlanski radiative condition is imposed for the 3D fields. A 150 km wide sponge layer with a viscosity of  $1000 \text{ m}^2 \text{ s}^{-1}$  along the open boundaries is also set up to damp outgoing eddies and waves.

### 2.3. Local Atmospheric Forcing

[13] In order to be consistent with PEN05 and MON10, the ROMS regional simulations were locally forced by a QuikSCAT monthly wind stress climatology computed from October 1999 to March 2003. Figure 1b displays the seasonal cycle of the alongshore wind stress climatology at three distinct latitudes on the Peruvian shelf. The wind forcing is upwelling favorable all yearlong with maximum intensity in austral winter. Two wind intensifications occur in May–June and September. The wind stress is stronger in the southern region of Peru, which encompasses a strong low-level atmospheric jet similar to the Chilean coastal jet [Garreaud and Mu  oz, 2005; Renault et al., 2009]. As a result one of the strongest upwelling cells of the Eastern South Pacific is observed between Pisco (14°S) and San Juan (16°S).

[14] Heat fluxes from COADS climatology [da Silva et al., 1994] were used. In order to account for air-sea feedbacks, a relaxation to COADS climatological sea surface temperature [da Silva et al., 1994] was imposed following the parameterization of Barnier et al. [1995] with a nudging coefficient varying spatially and temporally between  $20 \text{ W m}^{-2} \text{ }^\circ\text{C}^{-1}$  and  $40 \text{ W m}^{-2} \text{ }^\circ\text{C}^{-1}$ . To prevent salinity drift, we also imposed a relaxation to COADS sea surface salinity with a coefficient varying between  $7.4 \cdot 10^{-6} \text{ m s}^{-1}$  and  $8.6 \cdot 10^{-6} \text{ m s}^{-1}$ .

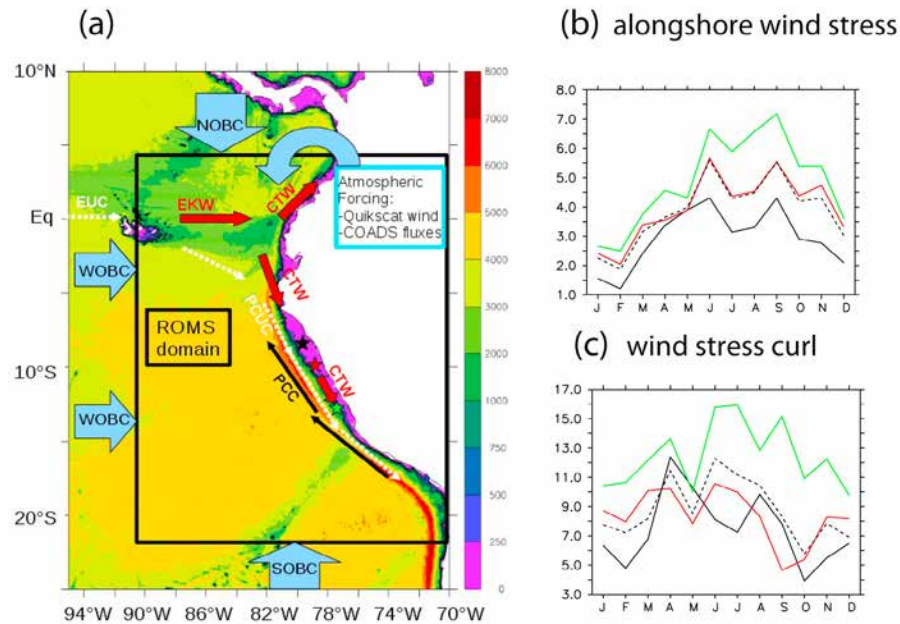


**Figure 1.** (a) ROMS model domain. Western, southern, and northern open boundary conditions (WOBC, SOBC, and NOBC, respectively, light blue arrows) from the OCCAM, SODA, ORCA OGCMs, QuikSCAT wind stress, and COADS heat fluxes (curved blue arrow) are the forcings of the model. The Equatorial Undercurrent (EUC, white dashed arrow west of the Galapagos Islands), Peru Coastal Current (PCC, solid black arrows), Peru Chile Undercurrent (PCUC, white dashed arrows), equatorial Kelvin waves (EKWs, red arrow along equator), and Coastal Trapped Waves (CTWs, red arrows along the Peru shore) pathways are also sketched. Background shading displays ETOPO2 bottom topography [Smith and Sandwell, 1997]. Black, red, and green stars indicate the position of the wind measurements shown in Figure 1b. (b) Seasonal variations of QuikSCAT alongshore wind stress (in  $10^{-2} \text{ N m}^{-2}$ ) at 8°S (black line), 11°S (red line), 13°S (green line), and averaged alongshore between 8°S and 13°S (dashed line). (c) Seasonal variations of QuikSCAT wind stress curl (in  $10^{-8} \text{ N m}^{-3}$ ) at 8°S (black line), 11°S (red line), 13°S (green line), and averaged alongshore between 8°S and 13°S (dashed line).

[15] Simulations were performed over a 10 year period, during which 5 day averages of the model outputs are stored. The first 3 years consist in a spin-up phase whereas the last 7 years correspond to the stabilized solution analyzed in this study. In the following, we refer to the Roccam/Rsoda/Rorca solution (and more generally to Rogcms) as the ROMS solution forced by the OCCAM/SODA/ORCA initial and boundary conditions.

[16] In order to assess the realism of the model results, we also used altimetric sea level data set from AVISO (<http://www.aviso.oceanobs.com/>) [Ducet *et al.*, 2000] and temperature and salinity fields from the 2001 World Ocean Atlas [Conkright *et al.*, 2002].

### 3. Results

#### 3.1. Zonal Circulation in the Near Equatorial Region

[17] The mean temperature and zonal currents at 86°W, downstream of the Galapagos Islands, are shown in Figure 2 to illustrate the mean equatorial inflow into the region. The three model solutions display the EUC centered near 0°S and at 60–80 m depth and a SSCC near 4°S and 100m depth, as with MON10. These results are consistent with the observed zonal circulation and thermal structure further west, at 90°W [see Kessler, 2006, Figure 9]. The EUC core velocity is very strong ( $\sim 35 \text{ cm s}^{-1}$ ) in Roccam, and weaker

and likely more realistic in Rsoda ( $\sim 15 \text{ cm s}^{-1}$ ) and Rorca ( $\sim 10 \text{ cm s}^{-1}$ ). The three simulations also exhibit SSCCs of similar magnitude near 4°S ( $\sim 10 \text{ cm s}^{-1}$ ) and 7–8°S ( $\sim 1 \text{ cm s}^{-1}$ ). The thermocline along the equator is well marked near 50 m depth in all the models, but the weak subsurface thermal stratification (or “thermostad”) observed at 90°W between  $\sim 100 \text{ m}$  and  $\sim 300 \text{ m}$  depth [Kessler, 2006], is only correctly simulated by Rsoda and Rorca (Figures 2b and 2c). In Roccam, subsurface thermal stratification is too strong due to a warm bias of  $\sim 1\text{--}2^\circ\text{C}$  in the upper 200 m (Figure 2a).

#### 3.2. Mean Structure of the Near-Coastal Current System

[18] Coastline effects, alongshore variations in bottom topography and mesoscale variability make difficult characterizing the NHCS at a single latitude. To minimize such effects and filter out part of the alongshore variability, temperature and velocity fields were averaged alongshore between 8°S and 13°S, a latitude band characterized by a relatively straight coastline (see Figure 1a). The annual mean currents of the three simulations in this latitude band only display small differences in the structure and intensity of the circulation (not shown). Thus, we focus on late austral winter (August–October) corresponding to the most intense upwelling period of the year (Figure 1b) during which the

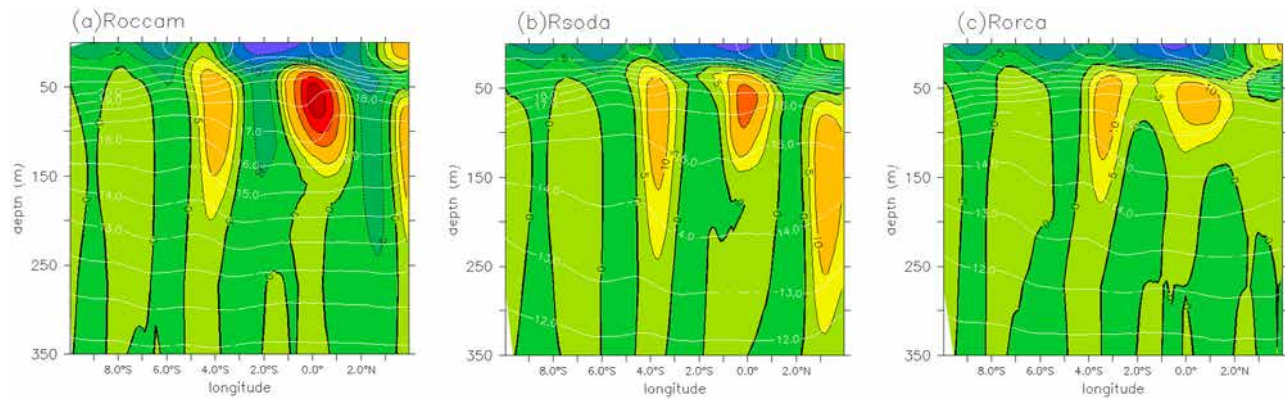


**Figure 2.** Temperature (in  $^{\circ}\text{C}$ , white contours) and zonal current (in  $\text{cm s}^{-1}$ , black contours and color scale) along  $86^{\circ}\text{W}$  in (a) Roccam, (b) Rsoda, and (c) Rorca. Solid (dashed) black contours indicate eastward (westward) flow. Contour interval for zonal velocity is  $5 \text{ cm s}^{-1}$  in the  $[-10, 10] \text{ cm s}^{-1}$  range and  $10 \text{ cm s}^{-1}$  elsewhere.

greatest discrepancies are observed. The resulting average cross-shore sections of temperature and meridional velocity are shown in Figures 3a–3c. A typical cross-shore section ( $10^{\circ}\text{S}$ ) of the SODA meridional velocity is also provided to illustrate the impact of the ROMS downscaling on the coastal current system structure (Figure 3d).

[19] The nearshore upward tilt of the isotherms indicates coastal upwelling. The offshore depth of the isotherms reaching the surface layer in the nearshore region corresponds approximately to the upwelling depth. This upwelling depth varies between  $\sim 60 \text{ m}$  in Rsoda and  $\sim 40 \text{ m}$  in Roccam and Rorca. The equatorward PCC is trapped within  $80 \text{ km}$  from the coast and extends from the surface down to the upwelling depth. This thin and shallow current exhibits maximum surface velocities of  $\sim 15 \text{ cm s}^{-1}$  in Roccam and Rorca, and of  $\sim 20 \text{ cm s}^{-1}$  in Rsoda. These structures contrast with those encountered in the SODA model (Figure 3d). The temperature and velocity structures shown at  $10^{\circ}\text{S}$  are typical of the OGCM solution. The upwelling depth is much greater ( $\sim 100\text{--}120 \text{ m}$ ) and the surface current is thicker ( $\sim 100\text{--}150 \text{ km}$ ) than in the Rsoda simulations. This partly results from the low-resolution ( $\sim 2^{\circ}$ ) ERA40 wind stress product forcing the SODA model, which does not correctly represent the drop-off observed in QuikSCAT near the coast. As a result, the near-coastal upwelling is likely overestimated in the SODA model. Note also the difference in the nearshore bottom topography, which leads to a thinner PCC in the ROMS simulations.

[20] Below the surface layer, the downward tilt of the isotherms corresponds to the depth of the poleward PCUC core, located between  $60 \text{ m}$  and  $120 \text{ m}$  along the continental slope. This subsurface current is found within  $\sim 120\text{--}140 \text{ km}$  from the coast, and exhibits a typical velocity of  $\sim 2\text{--}4 \text{ cm s}^{-1}$ . Despite similar annual mean characteristics (not shown), the PCUC core is shallower ( $\sim 60 \text{ m}$  against  $\sim 80\text{--}100 \text{ m}$ ) and stronger ( $\sim 4 \text{ cm s}^{-1}$  against  $\sim 2\text{--}3 \text{ cm s}^{-1}$ ) in Rorca than in Rsoda and Roccam. As it will be further investigated in section 3.5, these discrepancies in the PCUC characteristics are likely to be caused by the poleward propagation of CTWs. Note that the Roccam PCUC structure does not strongly differ from Rsoda even though the Roccam EUC flow is twice as large as that from the two other simulations

(Figure 2). This is consistent with the results of MON10, who showed using model Lagrangian diagnostics that the mass transfer between the EUC and the PCUC was very weak ( $1\text{--}2\%$  [see MON10, Table 2]). In contrast, these authors demonstrated that the main source of the PCUC are the SSCCs which show similar characteristics in the three simulations (see section 3.1 and Figure 2).

[21] The SODA PCUC (Figure 3d) strongly differs from the ROMS currents. The current's core is located offshore rather than on the slope, and at greater depths ( $\sim 140\text{--}160 \text{ m}$ ) than in ROMS. The differences in spatial resolution of the bottom topography and vertical discretization ( $z$  coordinates in SODA and  $\sigma$  coordinates in ROMS) may strongly modify the PCUC structure.

### 3.3. Seasonal Variability of the PCC and PCUC Transports

[22] The seasonal variations of the PCC and PCUC transports are now investigated. The PCC intensity is supposedly modulated by the temporal variability of the alongshore wind stress, which controls the intensity of the cross-shore density gradient. Given the seasonal variability shown in Figure 1b, the PCC transport is expected to be maximum during austral winter. On the other hand, the intensity of the poleward undercurrent should be strongly related to the local wind stress curl (Figure 1c) through Sverdrup transport as in other upwelling systems [Marchesiello *et al.*, 2003]. Furthermore, one may wonder if the eastward transport associated with the EUC, which very strongly contrasts between the simulations (Figure 4a), may partly control the PCUC poleward flow.

[23] Estimates of the PCC and PCUC transports were computed from the zonally averaged cross-shore section (see section 3.2). The PCC transport was computed by integrating the equatorward flow within  $150 \text{ km}$  from the coast and from the surface to  $100 \text{ m}$  depth (Figure 4b). The mean transport and its seasonal variability are weaker in Roccam and Rorca than in Rsoda. For all Rogcms the surface equatorward transport reaches a minimum value of  $\sim 0.1 \text{ Sv}$  during austral summer and fall, and a maximum in austral winter. Despite identical local atmospheric forcing in the three Rogcms, the austral winter PCC transport strongly varies among the Rogcms, being more than twice in Rsoda



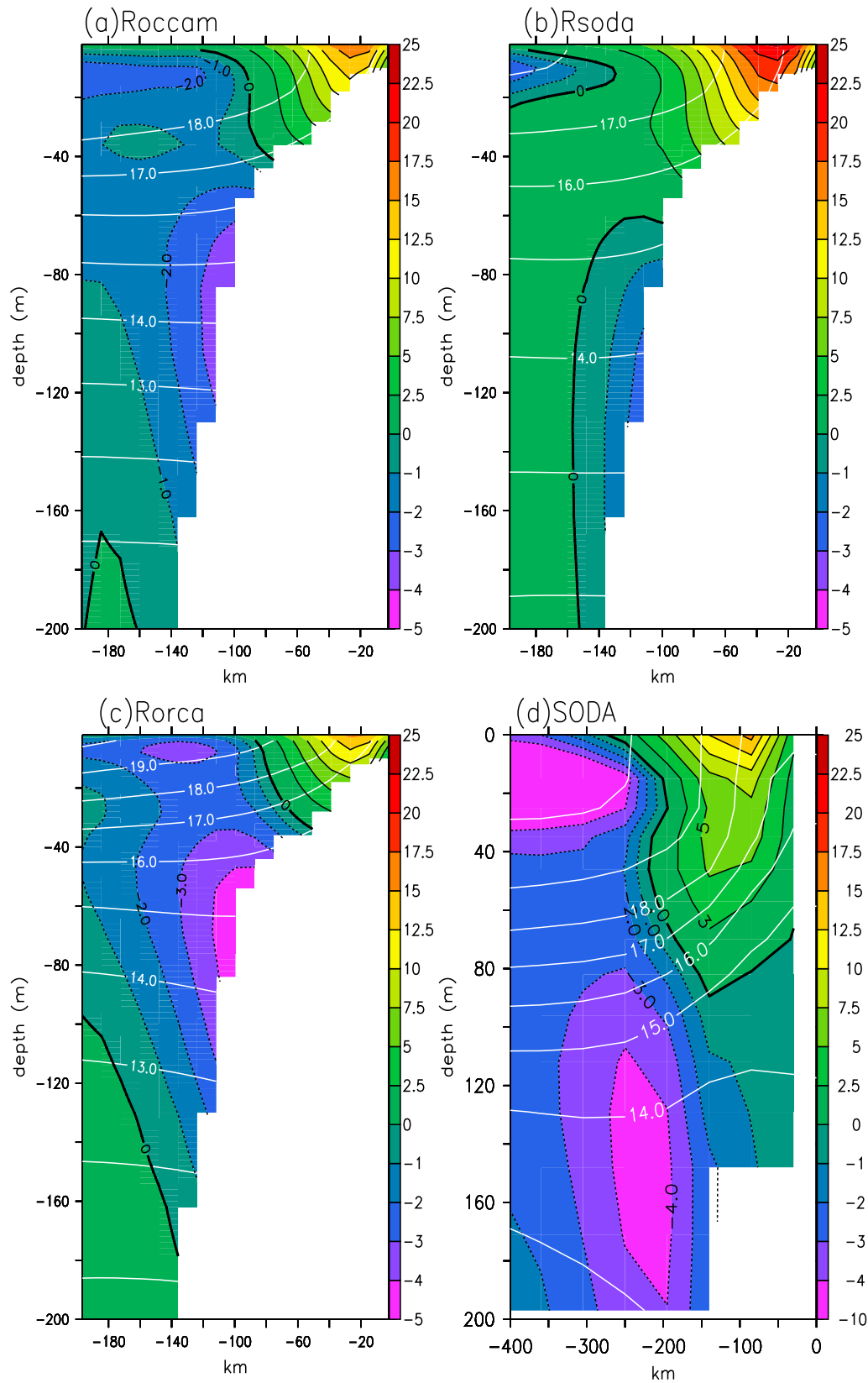


**Figure 3.** Temperature (in °C, white contours) and meridional velocity (in cm s<sup>-1</sup>, black contours and color) alongshore averaged between 8°S and 13°S for the period August–September–October in (a) Roccam, (b) Rsoda, and (c) Rorca. (d) SODA temperature and meridional velocity at 10°S (note the different cross-shore scale and color scale for poleward flow). Solid (dashed) black contours indicate equatorward (poleward) flow.

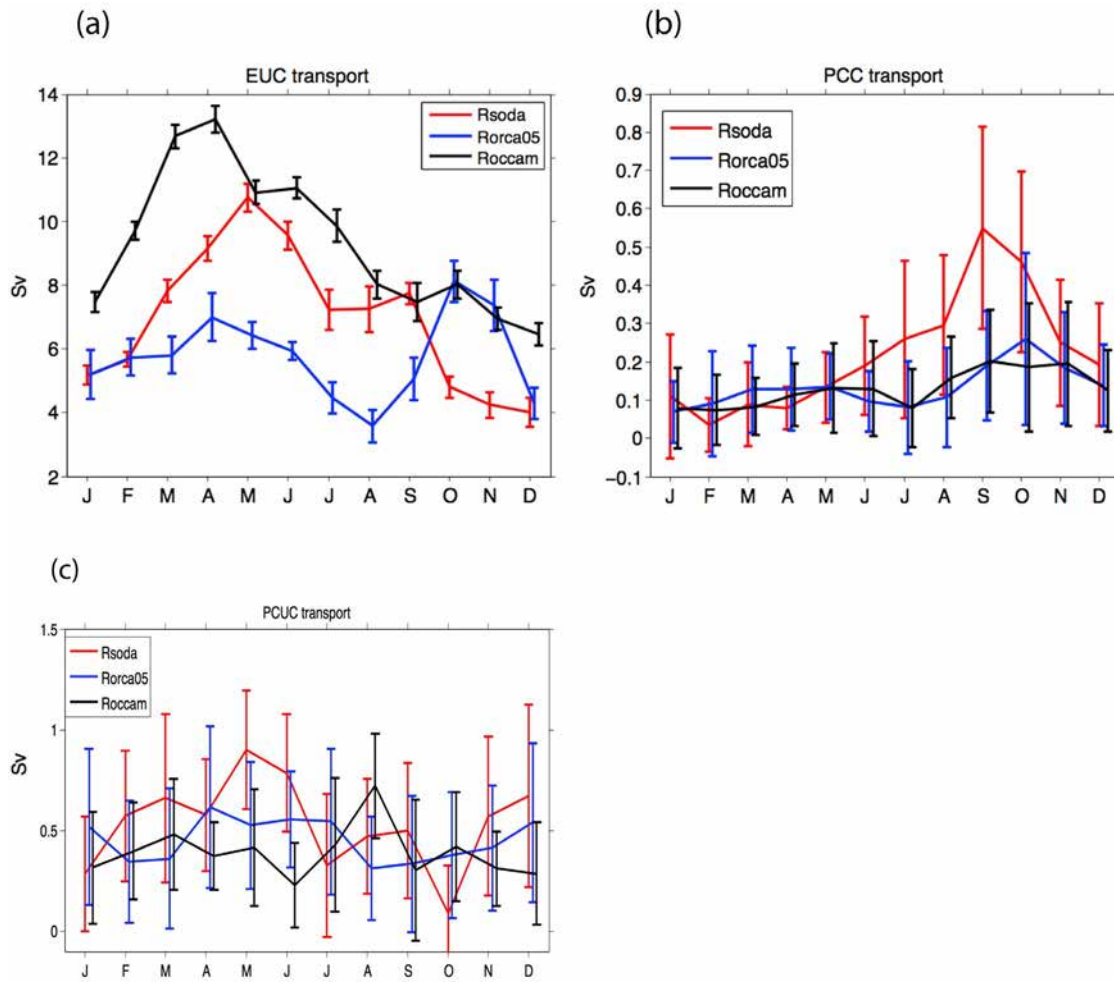


**Figure 4.** (a) EUC eastward transport (in Sv) through a meridional section at  $86^{\circ}\text{W}$ , between  $2^{\circ}\text{N}$  and  $2^{\circ}\text{S}$  and 300 m depth. (b) PCC equatorward transport (in Sv) through a 150 km wide, 100 m deep, zonal cross-shore section. Meridional velocities have been zonally averaged between  $8^{\circ}\text{S}$  and  $13^{\circ}\text{S}$ . Only equatorward velocities are taken into account. Bars correspond to  $\pm 1$  standard deviation around the mean, computed from the 7 year simulations. (c) PCUC poleward transport (in Sv) through a zonal cross-shore section. Meridional velocities have been zonally averaged between  $8^{\circ}\text{S}$  and  $13^{\circ}\text{S}$ . Only poleward velocities greater than  $1 \text{ cm s}^{-1}$ , between 20 and 300 m depth and from the coast to 200 km offshore, are taken into account. Bars correspond to  $\pm 1$  standard deviation around the mean, computed from the 7 year ROMS simulations. Color code is as follows: Rsoda is given in red, Rorca is given in blue, and Roccam is given in black.

( $\sim 0.5 \text{ Sv}$ ) than in Roccam and Rorca ( $\sim 0.2 \text{ Sv}$ ). Error bars in Figure 4b indicate that the variability of the PCC transport due to the intrinsic mesoscale circulation along the coast is of the same order of magnitude ( $\sim 0.1 \text{ Sv}$  for Roccam and Rorca and  $\sim 0.2 \text{ Sv}$  in Rsoda) than the seasonal variability.

[24] An estimate of the PCUC transport was computed by integrating poleward velocities greater than  $1 \text{ cm s}^{-1}$  in the 20–300 m depth range, within the 0–200 km coastal band (Figure 4c). In the three simulations, the mean PCUC transport is of  $\sim 0.5 \text{ Sv}$ . It has no straightforward relation to the EUC transport (Figure 4a), nor to the nearshore wind stress curl (Figure 1c). This lack of connection between the EUC and the PCUC corroborates the results of MON10. The seasonal variability of the PCUC transport differs among the Rogcms. Two relative maxima are observed in late austral spring (December) and fall (May–June) in Rorca and Rsoda,

whereas only one clear maximum is observed in austral winter (August) in Roccam. These variations seem to be partly connected to the EUC fluctuations in the case of Rorca and Rsoda. As for the PCC, the PCUC intrinsic variability is as large ( $\sim 0.5 \text{ Sv}$ ) as the seasonal variability, illustrating the strong impact of mesoscale activity.

[25] From this analysis, the PCUC transport appears to be driven by a complex combination of dynamical forcings. The local wind stress curl (Figure 1c) does not seem to constrain the PCUC transport. The EUC transport seems to play a role, but only in the Rorca and Rorca case, and during particular time periods.

### 3.4. Coastal Upwelling

[26] Coastal upwelling is one of the main characteristics of the NHCS. As for the PCC and PCUC, coastal upwelling

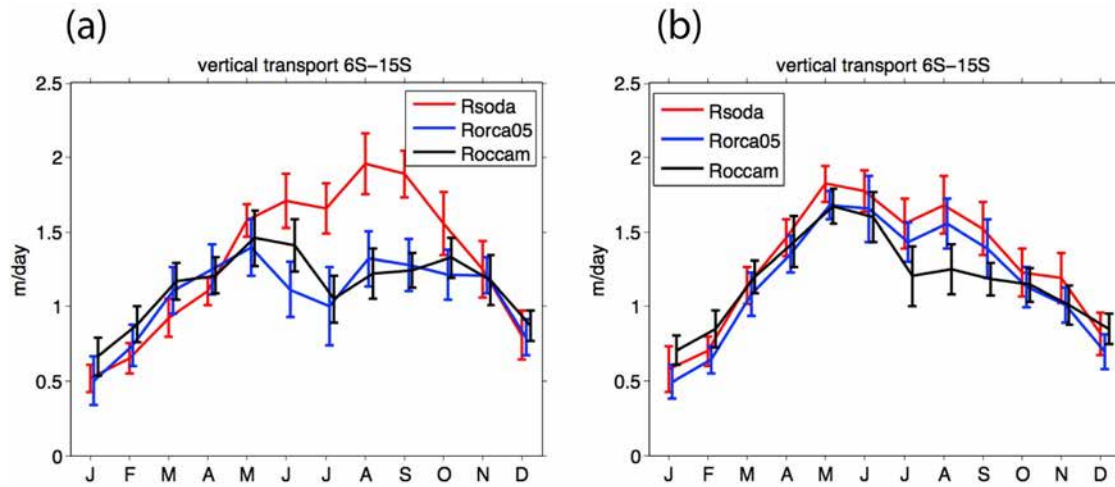


**Figure 5.** Vertical velocity (in  $\text{m d}^{-1}$ ) averaged over a  $6^{\circ}\text{S}$ – $15^{\circ}\text{S}$ , 100 km wide coastal box, for (a) Rogcm and (b) Rogcm-W (Rogcms simulations with fixed in time OBCs). Color code is as follows: Rsoda is given in red, Rorca is given in blue, and Roccam is given in black.

is driven by the alongshore wind stress through Ekman transport divergence at the coast, and by the nearshore wind stress curl through Ekman pumping [Capet *et al.*, 2004; Albert *et al.*, 2010]. The more the alongshore component (curl) of the wind stress intensifies, the stronger the upwelling of mass and nutrients. It is thus crucial to investigate the seasonal cycle of upwelling given the different Rogcms oceanic conditions.

[27] A coastal upwelling index (hereafter UI) was computed by averaging modeled vertical velocities at 50 m depth within a 100 km wide coastal band between  $6^{\circ}\text{S}$  and  $15^{\circ}\text{S}$  (Figure 5a). From November to May the Rogcms UIs are strikingly similar, showing a decrease between November ( $\sim 1.2 \text{ m d}^{-1}$ ) and January ( $\sim 0.6 \text{ m d}^{-1}$ ), followed by a rise until May ( $\sim 1.4 \text{ m d}^{-1}$ ). This indicates that during the season of moderate wind and increased stratification, the upwelling

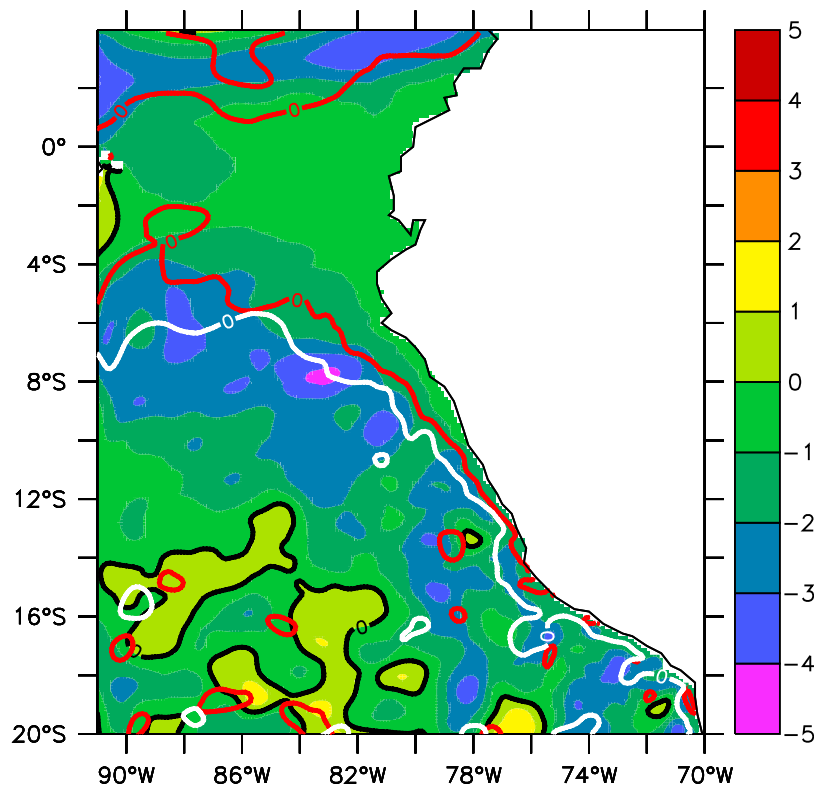


**Figure 6.** Rsoda sea level anomaly (in cm) in March (color scale and thick black contour for 0 cm isoline), April (thick red contour for 0 cm isoline), and May (thick white contour for 0 cm isoline). Anomalies are calculated with respect to the Rsoda-W simulation.

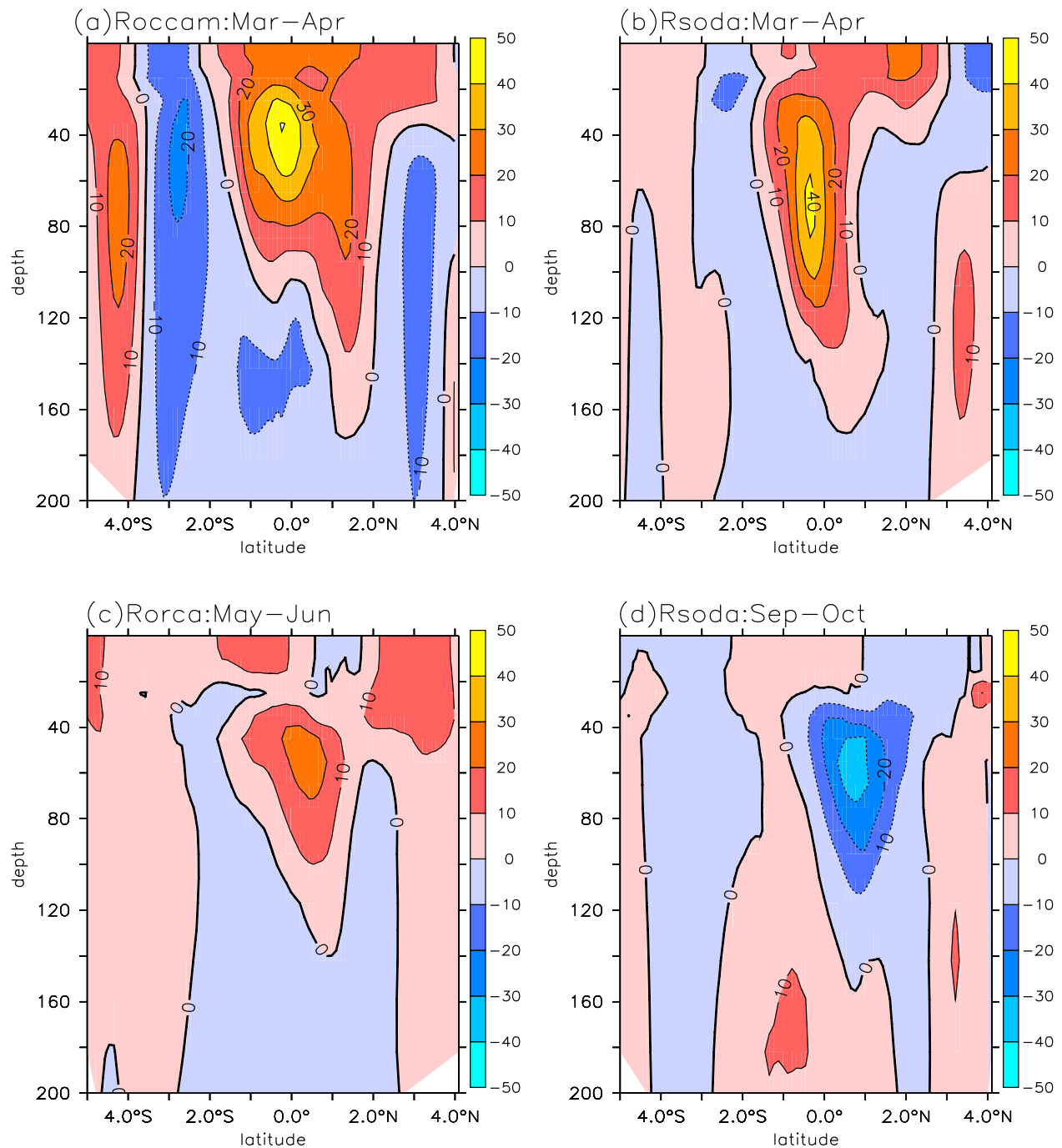


**Figure 7.** Zonal current anomalies (in  $\text{m s}^{-1}$ ) along  $86^\circ\text{W}$  associated to downwelling equatorial Kelvin waves in March–April for (a) Roccam and (b) Rsoda and (c) in May–June for Rorca and (d) upwelling equatorial Kelvin waves in September–October for Rsoda. Anomalies are calculated with respect to the Rogcm-W simulations. Positive anomalies correspond to eastward current.

intensity is mostly controlled by the wind and weakly depends on the large-scale ocean conditions. After May, UI stabilizes near  $\sim 1.2 \text{ m d}^{-1}$  in Rorca and Roccam, whereas it continues to increase in Rsoda, reaching a maximum of  $\sim 1.8 \text{ m d}^{-1}$  in August. This Rsoda upwelling increase is dynamically related to the increase in PCC transport (Figure 4b), as a stronger upwelling of subsurface dense water intensifies the cross-shore density gradient and the associated geostrophic along-shore surface current. In terms of annual mean integrated

upwelling flux, Rsoda upwells  $\sim 30\%$  more mass than other Rogcms despite the identical local wind forcing.

### 3.5. Impact of Equatorial Forcing on the Coastal Current System

[28] The impact of the seasonal variability of OBCs is studied as follows. First, we verified that the main influence of the OBCs derived from the  $[90^\circ\text{W}, 3^\circ\text{N}–3^\circ\text{S}]$  near-equatorial portion of the western open boundary, by running the model



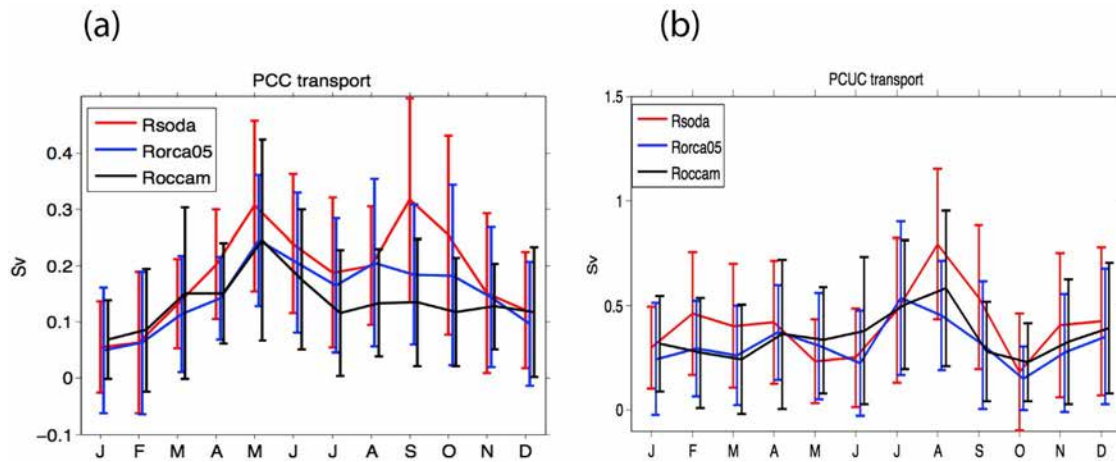


**Figure 8.** Seasonal variations of the (a) PCC and (b) PCUC transports in the case of the Rogcm-W simulations. Transports are defined in Figures 4b and 4c.

with time-constant OBCs everywhere but between 3°S and 3°N. We obtained similar PCUC, PCC and UI variations to those obtained with OBCs varying along the western, northern and southern open boundaries (not shown). This academic experiment proves that the main source of variability in the nearshore NHCS is provided by the equatorial waveguide.

[29] Modeled poleward propagating CTWs exhibit distinct characteristics depending on the OBC forcing. First, the phase and intensity of the CTWs are linked to the OGCM equatorial waves, which are triggered by the intraseasonal wind events in the western tropical Pacific Ocean [Madden and Julian, 1971, 1972]. Second, density stratification on the shelf and slope, which determines the vertical structure of the CTWs, is related to the water masses imposed by the OGCM and transported from the open boundaries into the coastal zone [MON10].

[30] A potential forcing of CTWs is the alongshore gradient of alongshore wind stress [Crépon and Richez, 1982] illustrated in Figure 1b. In order to separate the respective impact of the wind-forced and equatorially forced waves, simulations using annual mean, time-constant open boundary conditions were performed. They are referred to as Rogcm-W, the only time-dependent forcing in these experiments being the QuikSCAT wind stress and COADS heat fluxes. Computing anomalies by subtracting the model solutions forced by time-variable and by time-constant OBC removes the linear effect of wind-forced waves on the current system and allows emphasizing the role of CTWs of equatorial origin.

[31] Figure 6 illustrates the sea level anomaly corresponding to the propagation of a downwelling wave (associated with a positive sea level anomaly) during austral fall (March–April–May) in the Rsoda simulation. The temporal variation of the anomalous pattern is typical of an EKW propagating eastward and generating poleward propagating CTWs. In March, the anomaly is confined south of the Galapagos, near [0°S–4°S, 90°W]. One month later (April), it has propagated along the equator and along the coasts of Ecuador and Peru (up to 15°S). In May, the sea level positive anomaly has reached the southern boundary of the model (22°S). Similar patterns are obtained for the other Rogcms during different time periods (not shown).

[32] Eastward current anomalies in the equatorial band [4°S, 4°N] at 86°W are shown in Figure 7 for different time periods corresponding to Kelvin wave propagation events. The different dates were chosen to highlight the current anomalies at the passage of the waves, which do not propagate simultaneously in the Rogcms. In April–May an eastward current anomaly of  $\sim 30 \text{ cm s}^{-1}$  associated with a so-called “downwelling” (related with a positive sea level anomaly, not shown) equatorial Kelvin wave is evidenced in Roccam and Rsoda (Figures 7a and 7b). This subsurface eastward current anomaly in the equatorial region generates a poleward surface coastal current along the Peru shore (not shown). Similarly, a weaker eastward anomaly of  $\sim 20 \text{ cm s}^{-1}$  is observed in May–June in Rorca (Figure 7c), related to the passage of a downwelling Kelvin wave. In austral winter, an upwelling EKW associated with a westward current anomaly of  $\sim 30 \text{ cm s}^{-1}$  at 86°W is only observed in Rsoda (Figure 7d). Note that these waves have a maximum current anomaly near 40–80 m depth and a weak impact in the 0–20 m surface layer, suggesting the evidence of second and possibly higher-order baroclinic modes.

[33] The different timing of the OGCM waves partly explains the PCC transport discrepancies between the Rogcms. In the case of time-constant OBC, the PCC transport peaks in May ( $\sim 0.25$ – $0.3 \text{ Sv}$ , Figure 8a), consistently with the wind strengthening in austral fall (Figure 1b). Thus, the weaker PCC transport during March–April evidenced in the three Rogcms ( $\sim 0.08$ – $0.12 \text{ Sv}$ , Figure 4b) is mainly caused by remotely forced downwelling CTWs, which generate a poleward surface current opposed to the equatorward, wind-forced PCC.

[34] During austral fall and winter, the Rsoda PCC transport reduces from  $\sim 0.5$  (Figure 4c) to  $\sim 0.3 \text{ Sv}$  (Figure 8a) when the austral winter upwelling EKW is filtered out from the OBCs. Nevertheless, the effect of this wave cannot fully account for the PCC transport differences among the Rogcms, as it remains  $\sim 30\%$  ( $\sim 50\%$ ) higher in Rsoda-W than in Rorca-W (Roccam-W) in September.

[35] Alongshore subsurface currents associated to baroclinic CTWs [Brink, 1982] may also modify the PCUC transport. Its seasonal variability becomes very similar once equatorial waves are filtered from OBCs (Figure 8b). The transport displays weak seasonal variations ( $\sim 0.1$ – $0.2 \text{ Sv}$ ) although it

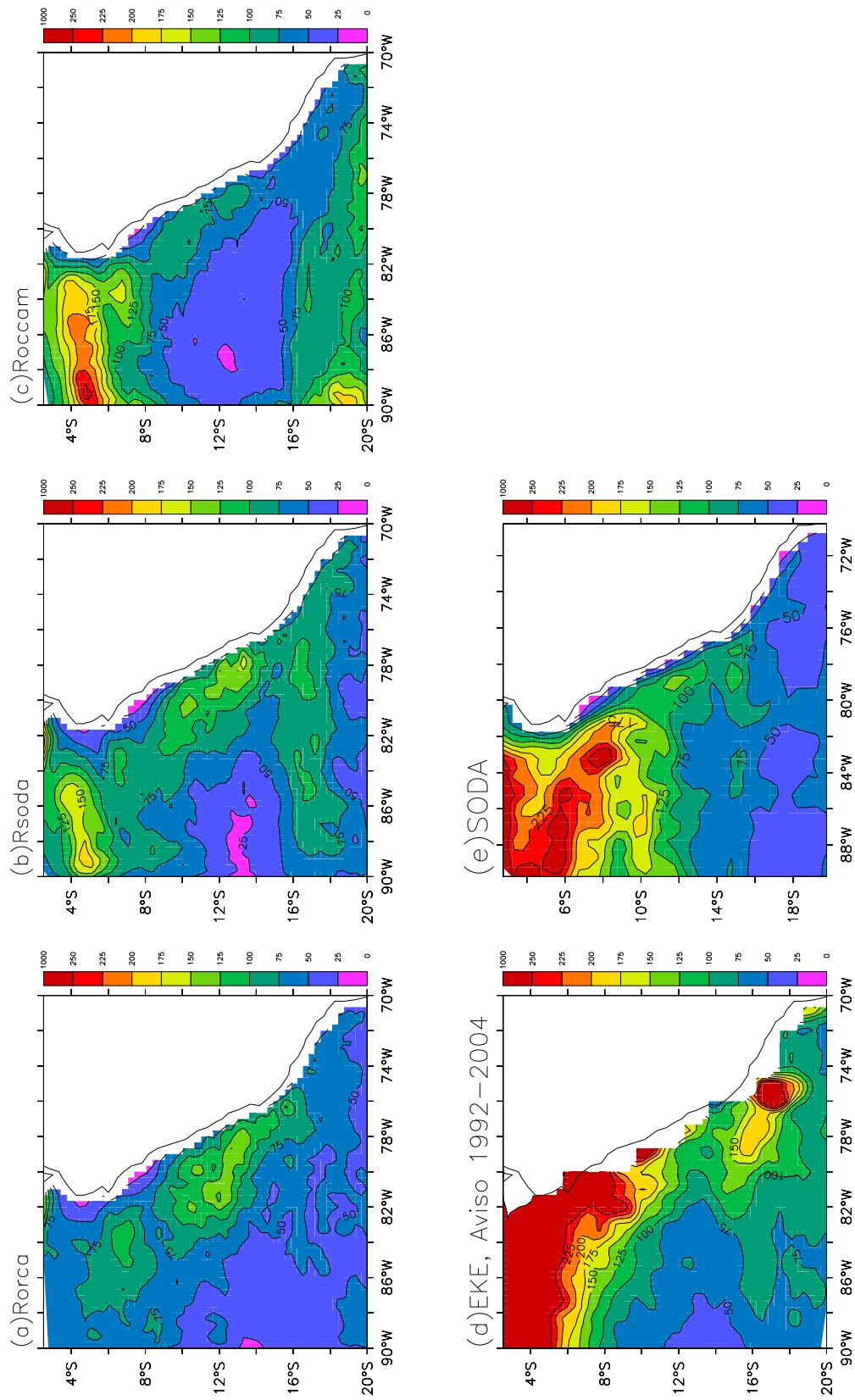


**Figure 9.** Mean eddy kinetic energy (EKE, in  $\text{cm}^2 \text{s}^{-2}$ ) in (a) Rorca, (b) Rsoda, (c) Roccam, (d) 1992–2005 AVISO observations, and (e) 1980–2000 SODA model.

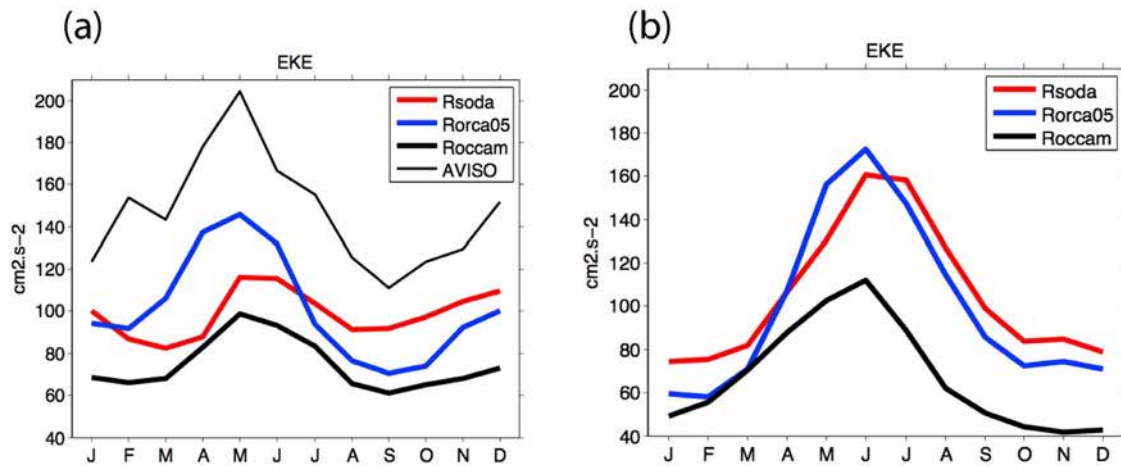


**Figure 10.** Seasonal cycle of EKE (in  $\text{cm}^2 \text{s}^{-2}$ ) averaged over a 400 km wide coastal band between  $8^\circ\text{S}$  and  $13^\circ\text{S}$  for (a) Rogcms and for (b) Rogcms-W simulations. Color code is as follows: AVISO is the thin black line in Figure 10a, Roccam is the thick black line, Rsoda is the thick red line, and Rorca is the thick black line.

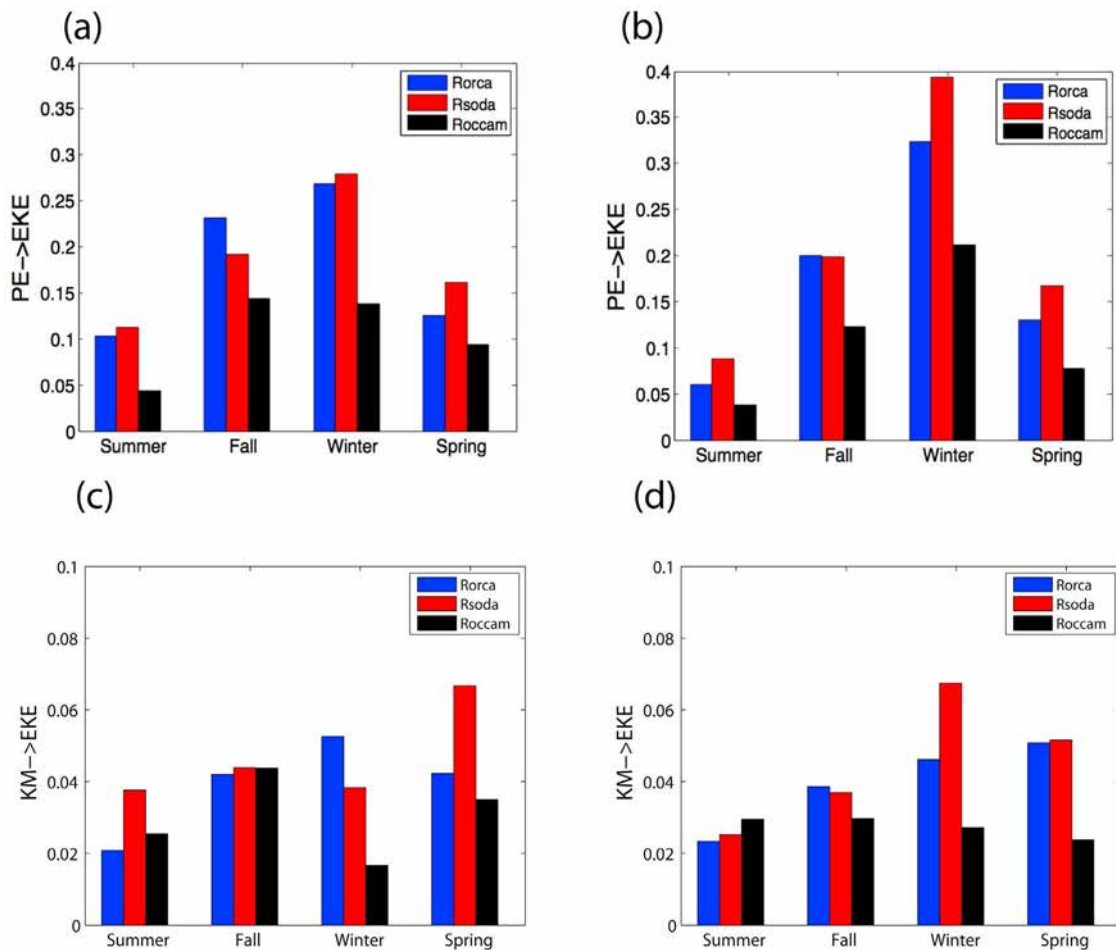


**Figure 11.** Potential energy (PE) to EKE energy flux (in  $10^8 \text{m}^2 \text{s}^{-3}$ ) for (a) Rogcms and (b) Rogcms-W. Mean kinetic energy (KM) to EKE energy flux (in  $10^8 \text{m}^2 \text{s}^{-3}$ ) for (c) Rogcms and (d) Rogcms-W. Fluxes were calculated for each season (3 months) and averaged over the 0–200 m depth range, in a coastal box of 400 km width, and over the  $8^\circ\text{S}$ – $15^\circ\text{S}$  latitude range.

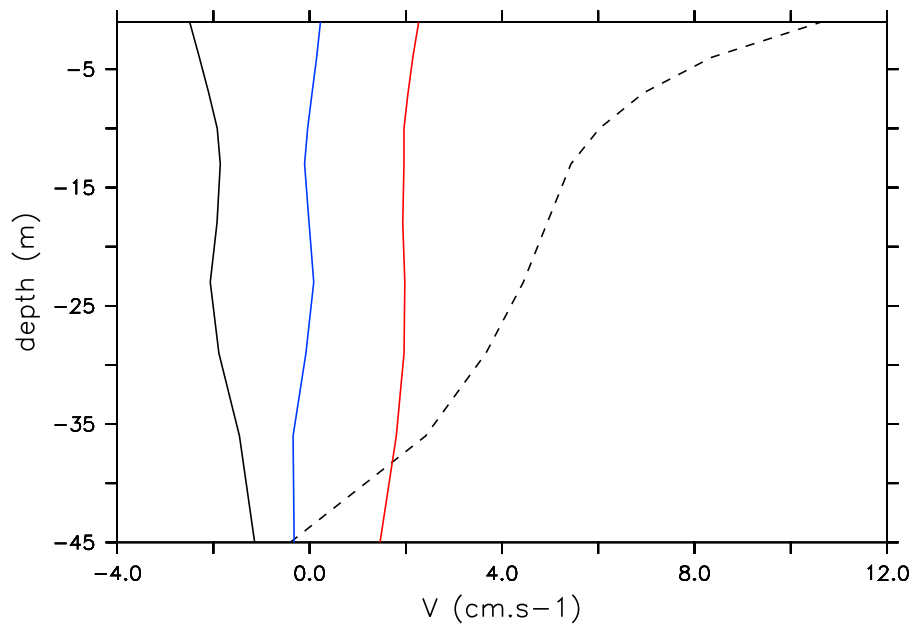


**Figure 12.** Vertical profile of the Rogcm alongshore-averaged meridional current (in  $\text{m s}^{-1}$ ), 60 km from the coast (black dashed line) and differences between the mean profile and each Rogcm profile (solid lines: Roccam-W (black), Rsoda-W (red), and Rorca-W (blue)). Currents have been averaged for the austral winter period (August–September–October).

reaches a marked maximum in July–August ( $\sim 0.75$ ,  $\sim 0.6$ , and  $\sim 0.4$  Sv in Rsoda, Roccam, and Rorca, respectively). The strong variations observed in Rsoda in June and October (Figure 4c) are no longer present. Accordingly, UIs are also strongly impacted by EKW and CTWs (Figure 5b). When filtered, UIs from the various Rogcms differ very little, except during austral winter as the Rsoda UI remains slightly higher ( $\sim 1.6 \text{ m d}^{-1}$ ) than in the two other simulations ( $\sim 1.5 \text{ m d}^{-1}$  in Rorca and  $\sim 1.3 \text{ m d}^{-1}$  in Roccam).

### 3.6. Mean and Seasonal Variability of Eddy Kinetic Energy

[36] Simulated surface eddy kinetic energy (EKE) is compared with the EKE derived from the AVISO sea level data set. The EKE from the SODA model is also shown to illustrate the impact of the regional downscaling on mesoscale activity. Sea level anomalies were computed with respect to a 7 year monthly climatology in the Rogcms, with respect to a 13 year (1993–2005) monthly climatology from AVISO observations, and with respect to a 1980–2000 monthly climatology in SODA. Note that our EKE index filters out the seasonal kinetic energy, such as for instance that of seasonal CTW and seasonally forced eddies, and includes only the energy of nonseasonal eddies. Since submesoscale eddies cannot be captured from satellite altimetry [Chaigneau *et al.*, 2008], modeled sea level anomalies were linearly interpolated onto a  $1/4^\circ \times 1/4^\circ$  spatial grid, at the same resolution than the AVISO product. Sea level slopes were then computed to derive surface geostrophic currents. Note that the inclusion or not of data from the 1997–1998 ENSO time period in the AVISO and SODA data sets did not significantly modify the mean EKE patterns, intensity and seasonality (not shown).

[37] EKE spatial patterns are displayed in Figure 9. As in the observations, the ROMS EKE shows higher values in

the  $\sim 200$ – $400$  km wide coastal band than offshore. South of  $6$ – $8^\circ\text{S}$ , the mean EKE in the Rogcms (Figures 9a–9c) is of the same order of magnitude than the AVISO product (Figure 9d), with typical values of  $50$ – $150 \text{ cm}^2 \text{ s}^{-2}$ . North of  $6$ – $8^\circ\text{S}$  in the tropics, important discrepancies between Rogcms and observed EKE spatial distributions are noted. For instance in Rorca (Figure 9a), low EKE values of  $\sim 75$ – $100 \text{ cm}^2 \text{ s}^{-2}$  in the  $2^\circ\text{S}$ – $5^\circ\text{S}$  latitude band contrast with EKE values higher than  $300 \text{ cm}^2 \text{ s}^{-2}$  observed in AVISO (Figure 9d). These highly energetic levels, associated with the intense intraseasonal wave activity of the equatorial

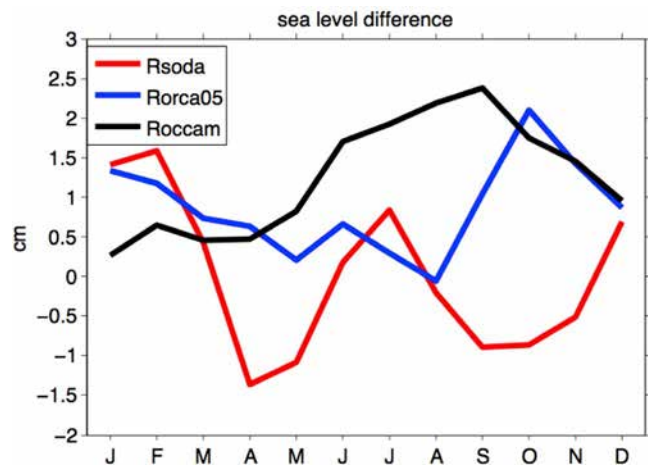


**Figure 13.** Sea level difference (in cm) between  $8^\circ\text{S}$  and  $13^\circ\text{S}$  for Roccam-W (black line), Rsoda-W (red line), and Rorca-W (blue line). A positive sea level difference induces an onshore geostrophic current which partly compensates Ekman transport and reduces the cross-shore sea level slope.



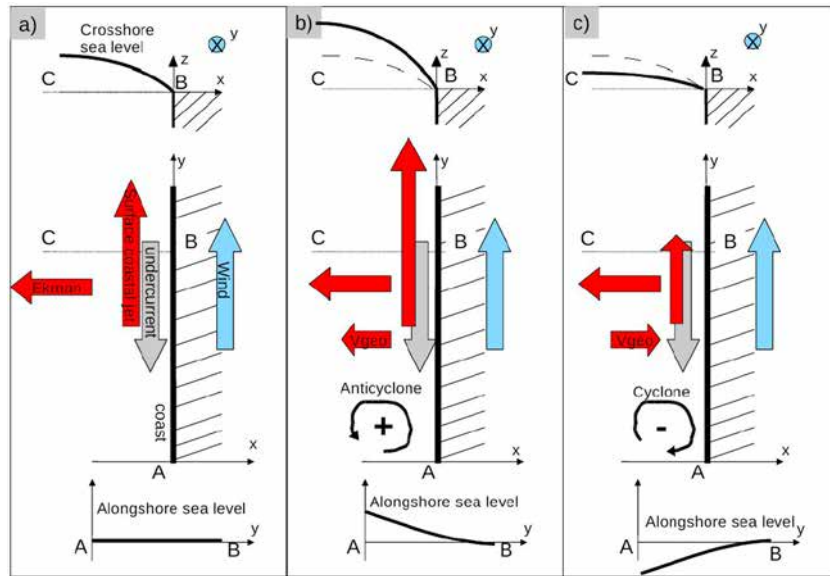


**Figure 14.** Sketch of the (middle)coastal current system, (top) cross-shore, and (bottom) along-shore sea level profile in presence of eddy-related sea level anomalies. (a) Normal situation, featuring an equatorward surface coastal jet (red arrow), poleward undercurrent (gray arrow), offshoreward Ekman current (red arrow), and equatorward wind (blue arrow). (b) Circulation in presence of an anticyclonic coastal eddy near coastal location A. The eddy generates a sea level rise near A. A poleward pressure gradient between A and B forces an offshoreward geostrophic current ( $V_{geo}$ , red arrow) which adds to the Ekman flow. The enhanced offshoreward flow increases the sea level depression at the coast (top view) and the associated cross-shore pressure gradient, thus increasing the equatorward surface jet. (c) Circulation in presence of cyclonic coastal eddy (i.e., negative sea level anomaly) near location A.

region, are reduced in the simulations forced by monthly climatological OBC. The high EKE in the tropics is relatively well reproduced in the SODA interannual simulation (Figure 9e). However, as SODA is only an eddy-permitting OGCM, EKE is relatively low along the coast, particularly in the Pisco–San Juan upwelling region (14–16°S).

[38] Figure 10a shows the EKE seasonal variability, averaged over a coastal band of 400 km width off central Peru (between 8°S and 13°S), encompassing the energetic coastal zone. The modeled EKE range of  $\sim 80\text{--}100\text{ cm}^2\text{ s}^{-2}$  is lower than the observed values ( $\sim 140\text{--}200\text{ cm}^2\text{ s}^{-2}$ ). However, observed and modeled seasonal variations are qualitatively in phase despite the different OBC forcing. EKE peaks in April–May in AVISO and Rorca, and in May–June in Rsoda and Roccam. A secondary maximum is attained in austral summer (December–January), whereas minimum values are reached in August–September both in the Rogcms and observations. Rather surprisingly, the different timing of the OBC EKW does not significantly impact the EKE phase. Note also that the amplitude of the Rorca EKE variations is quite realistic despite the spatial bias shown in Figures 9a–9d.

[39] The EKE seasonal variations are strongly impacted by the presence of EKW and CTW. When filtered, the EKE amplitude increases and its phase is locked on the wind seasonal cycle in each Rogcm (Figure 10b). The EKE maximum is shifted in time toward austral winter by  $\sim 1$  month. During austral winter, the EKE increase is particularly intense ( $\sim 33\%$ ) in Rsoda-W compared to Rsoda, and more moderated in Rorca-W ( $\sim 20\%$ ) and Roccam-W ( $\sim 10\%$ ). In austral spring and summer, EKE decreases by  $\sim 30\%$  in Roccam-W and Rsoda-W, and by  $\sim 15\%$  in Rsoda-W. Thus, the EKE seasonal

cycle amplitude increases by a minimum of  $+75\%$  in Roccam to a maximum of  $+100\%$  in Rsoda when using time-constant OBC. Note also that the secondary austral summer EKE maximum (Figure 10a) is absent in the Rogcms-W.

[40] Quantification of energy fluxes from mean state to perturbations helps identifying the instability processes at stake (Figure 11). For a mathematical definition of these terms, readers are referred to Marchesiello *et al.* [2003]. Energy fluxes were computed for each season and averaged over the same coastal band than in Figure 10. Potential energy (PE) to EKE flux (Figures 11a and 11b) is much greater than mean kinetic energy to EKE flux (Figures 11c and 11d), particularly in austral winter, indicating a greater efficiency of baroclinic instability than barotropic instability to transfer energy to eddies. The PE to EKE flux is lowest in Roccam, consistently with the low mean EKE level in this simulation (Figures 9c–10a). During austral summer and fall, the PE to EKE flux is higher in the Rogcms (Figure 14a) than in the Rogcms-W (Figure 14b). In contrast during austral winter, the flux is  $\sim 25\%$  (Rorca) to  $\sim 50\%$  (Rsoda) greater in Rogcm-W simulations (Figure 14b), consistently with Figure 13. Note that the PE to EKE fluxes fluctuate in phase and peak in austral winter in all Rogcm-W simulations.

[41] The effect of the OBC time variability on the current system instabilities suggests the following interpretation: CTWs destabilize the current as passing waves tilt near-shore isopycnals up and down in austral spring and summer, when the wind-driven upwelling is relatively weak. An EKE burst occurs in austral fall when the upwelling intensifies. In the Rogcms-W without CTWs, nearshore isopycnals remain relatively flat until the beginning of the upwelling

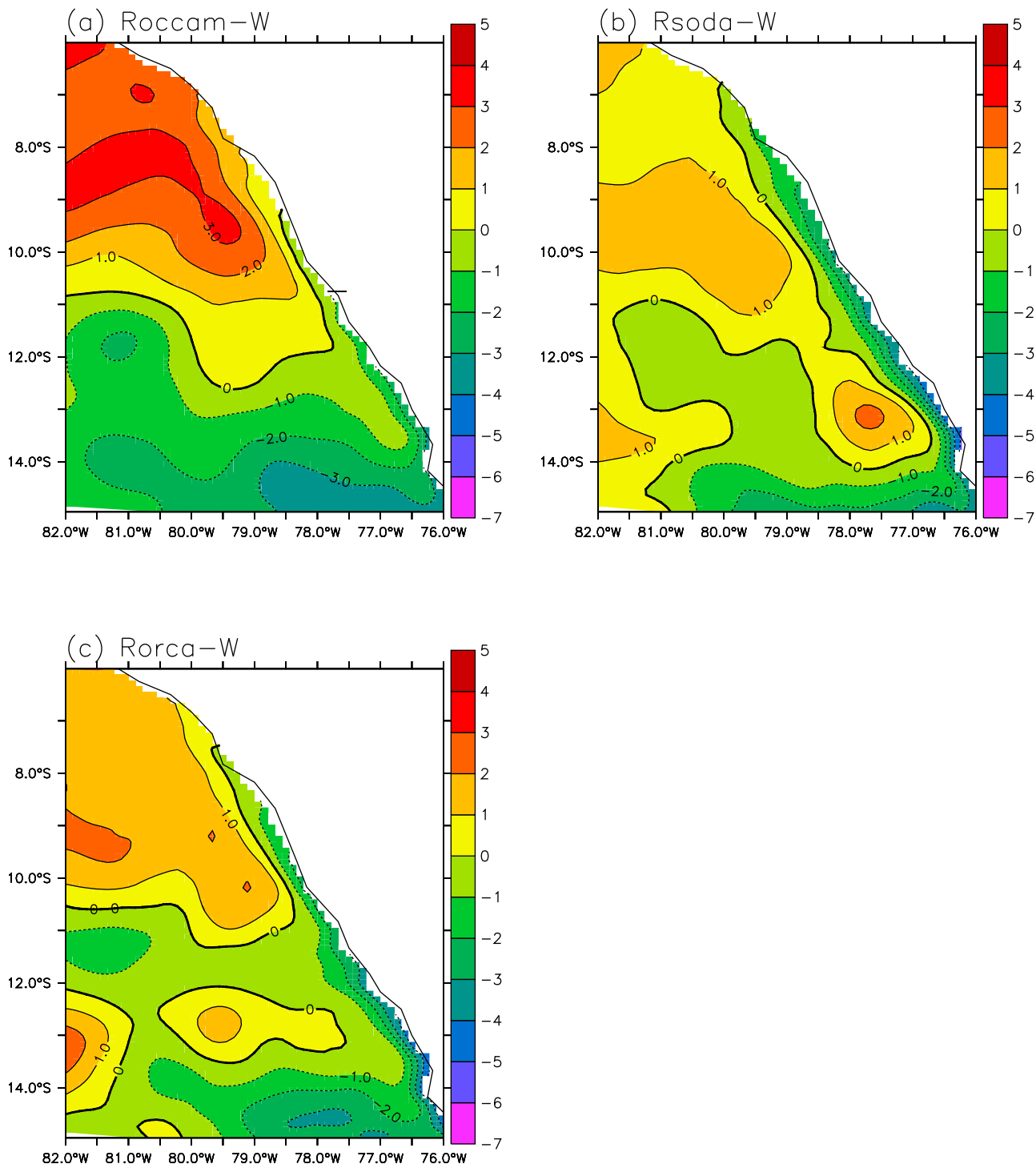


**Figure 15.** Average sea level (in cm) in September for (a) Roccam-W, (b) Rsoda-W, and (c) Rorca-W.

season. PE increases only in late fall to early winter, which triggers baroclinic instability and eddy generation during austral winter.

#### 4. Discussion

[42] Comparing model simulations with and without the influence of OBC time variability emphasizes the impact of

seasonal EKW on the NHCS nearshore circulation. PCUC transport variations strongly depend on the timing and amplitude of the incoming CTWs (Figure 4c). In contrast, they become comparable without CTWs (Figure 8b), suggesting control by the local wind stress [Ramos *et al.*, 2006]. Discrepancies between the Rogcms PCUC fluxes may also ensue from the different time periods chosen to construct the monthly climatological forcing from the various OGCMs

outputs (see section 2). The equatorial Pacific is crossed by trains of intraseasonal EKW [Cravatte *et al.*, 2003] which are modulated interannually [Dewitte *et al.*, 2008]. Monthly averaging of OGCM density and current fields performed over several yearlong time periods filters most of the non-seasonal propagating waves. Unlike the ORCA and SODA simulations, the OCCAM simulation (also used by PEN05 and MON10) was forced by a monthly climatology of ECMWF wind stress from a very short time period (1986–1988). As a result, an important weight is given to the intraseasonal wind bursts triggering EKW during this particular 2 year period, and the resulting waves are not in phase with the seasonal EKW obtained from the ORCA and SODA 10 year climatologies. This artifact could explain why EKW, and hence CTWs and PCUC transport, are so different in Roccam than in the other two solutions.

[43] Nevertheless, the EKW forcing discrepancies do not fully explain the differences in PCC transport and upwelling intensity. When EKW are filtered, the PCC transport, upwelling intensity and local wind forcing vary approximately in phase, but the austral winter values remain dependant on the mean large-scale density field set by the time average boundary and initial conditions. In austral winter, vertical profiles of alongshore velocity in the PCC core show that Rogcms-W coastal currents differ mainly by a barotropic component (Figure 12). The alongshore sea level difference, at the offshore limit of the coastal zone (see section 3.2) between 8°S and 13°S, is a plausible forcing of this barotropic current (Figure 13). The sea level gradient generates an alongshore surface pressure gradient acting on the alongshore momentum balance. All yearlong and particularly in late austral winter to early spring, the pressure gradient is oriented poleward in Roccam and Rorca, forcing a coastward geostrophic flow opposite to the offshoreward Ekman flow as observed during the 1997–1998 El Nino Southern Oscillation event [Colas *et al.*, 2008]. This current piles up water near the coast, increasing the coastal sea level, and decreasing the cross-shore sea level slope. In turn, this cross-shore sea level slope decrease leads to a reduced geostrophically balanced alongshore equatorward flow. This sequence of mechanisms, summarized in Figures 14a–14c, occurs in Roccam (July–December) and Rorca (September–January). On the other hand, the opposite sequence of mechanisms occurs in Rsoda (in austral fall and late winter to early spring), resulting in an enhanced equatorward flow (Figure 14b).

[44] The dynamical forcing generating the alongshore pressure gradient remains to be investigated. Figure 15 displays the sea surface topography for the Rogcms-W in September. In this time period, an anticyclonic eddy is generated near ~13°S in Rsoda, and propagates westward during the following months (not shown). The positive sea level anomaly associated to the eddy thus generates a strong equatorward pressure gradient.

[45] This phenomenon may play a major role when coastal eddies are associated with strong sea level anomalies. It could be enhanced in the real ocean, as nearshore mesoscale activity is slightly underestimated in our simulations (Figures 9 and 10). The timing and position of such eddies could be determined by complex, nonlinear eddy generation mechanisms related to interactions between wind

forcing, local density stratification driven by large-scale density gradients, bottom topography and coastline effects [Marchesiello *et al.*, 2003]. The study of these mechanisms is beyond the scope of this work. Finally, intraseasonal EKW, which are damped in our climatological simulations, may play a similar dynamical role than the seasonal EKW, which remains to be investigated. In conclusion, the nonlinear mechanism evidenced in this work may enhance or mitigate the wind-driven upwelling, depending on the vorticity and position of the mesoscale eddies. This could strongly modulate the biological productivity of the upwelling system.

## 5. Conclusions

[46] Initial and boundary conditions imposed by OGCMs strongly influence the dynamics of regional circulation models. In this work, we investigated the particular case of the Northern Humboldt Current System, one of the four major Eastern Boundary Upwelling Systems of the world ocean. Three different OGCMs were used to initialize and drive the ROMS regional ocean circulation model at its open boundaries. They impose different initial density stratifications, phasing and intensity of seasonal eastward propagating equatorial Kelvin waves, which generate poleward propagating coastal-trapped waves associated with alongshore surface and subsurface coastal currents. The equatorward transport and the nearshore upwelling are mostly related to the wind forcing, whereas the undercurrent transport is mostly modulated by the OBC forcing.

[47] The incoming waves also impact the amplitude and phase of seasonal mesoscale activity. It is maximum in austral fall and spring when EKW are present, and agrees qualitatively with mesoscale activity derived from altimetric observations. In contrast, mesoscale activity peaks in early austral winter when EKW are filtered, during the period of intensified winds. The intrinsic variability of the PCC and PCUC transports is related to mesoscale eddies and is as high as the seasonal variability. This highlights the difficulty to monitor coastal flows over short time periods and at single cross-shore sections.

[48] The phase and intensity of the surface flow and upwelling also depend on nonlinear processes, such as the development of nearshore mesoscale eddies through baroclinic instability processes. Seasonal coastal eddies may be generated by instabilities of the current system at the passage of coastal waves or due to the local density stratification forced by boundary conditions. The sea level anomalies associated to the eddies force alongshore surface pressure gradients, which modulate the alongshore surface flow. This mechanism illustrates the important nonlinear role of large-scale density gradients set by the regional model initial and boundary conditions.

[49] **Acknowledgments.** We acknowledge three anonymous reviewers for their useful comments and Gurvan Madec and Michel Crépon from LOCEAN for fruitful discussions during the correction of this manuscript. Numerical computations were performed on the NEC-SX8 of the IDRIS (Institut du Développement et des Ressources en Informatique Scientifique) center and at the National Center for Supercomputer Applications (NCSA). V. Echevin, A. Chaigneau, and P. Penven are sponsored by IRD (Institut de Recherche pour le Développement). F. Colas was partly sponsored by the ATI Sistema de Humboldt funded by IRD.

## References

- Albert, A., V. Echevin, M. Lévy, and O. Aumont (2010), Impact of near-shore wind stress curl on coastal circulation and primary productivity in the Peru Upwelling System, *J. Geophys. Res.*, **115**, C12033, doi:10.1029/2010JC006569.
- Barnier, B., L. Siefridt, and P. Marchesiello (1995), Thermal forcing for a global ocean circulation model using a three-year climatology of ECMWF analyses, *J. Mar. Syst.*, **6**, 363–380, doi:10.1016/0924-7963(94)00034-9.
- Brink, K. H. (1982), A comparison of long coastal trapped wave theory with observations off Peru, *J. Phys. Oceanogr.*, **12**, 897–913, doi:10.1175/1520-0485(1982)012<0897:ACOLCT>2.0.CO;2.
- Brochier, T., C. Lett, J. Tam, P. Freon, F. Colas, and P. Ayon (2008), An individually based model study of Anchovy early life in the Northern Humboldt Current System, *Prog. Oceanogr.*, **79**, 313–325, doi:10.1016/j.ocean.2008.10.004.
- Capet, X. J., P. Marchesiello, and J. C. McWilliams (2004), Upwelling response to coastal wind profiles, *Geophys. Res. Lett.*, **31**, L13311, doi:10.1029/2004GL020123.
- Carton, J. A., and B. S. Giese (2008), A reanalysis of ocean climate using Simple Ocean Data Assimilation (SODA), *Mon. Weather Rev.*, **136**, 2999–3017.
- Chaigneau, A., A. Gizolme, and C. Grados (2008), Mesoscale eddies off Peru in altimeter records: Identification algorithms and eddy spatio-temporal patterns, *Prog. Oceanogr.*, **79**, 106–119, doi:10.1016/j.pcean.2008.10.013.
- Chavez, F. P., A. Bertrand, R. Guevara-Carrasco, P. Soler, and J. Csirke (2008), The Northern Humboldt Current: Brief history, present status and a view towards the future, *Prog. Oceanogr.*, **79**, 95–105.
- Clarke, A. J. (1983), The reflection of equatorial waves from oceanic boundaries, *J. Phys. Oceanogr.*, **13**, 1193–1207, doi:10.1175/1520-0485(1983)013<1193:TROEWF>2.0.CO;2.
- Colas, F., X. Capet, J. C. McWilliams, and A. Shchepetkin (2008), 1997–1998 El Niño off Peru: A numerical study, *Prog. Oceanogr.*, **79**, 138–155, doi:10.1016/j.pcean.2008.10.015.
- Conkright, M. E., R. A. Locarnini, H. E. Garcia, T. O'Brien, T. P. Boyer, C. Stephens, and J. I. Antonov (2002), World ocean atlas 2001: Objective analyses, data statistics, and figures [CD-ROM], *Intern. Rep.* **17**, 17 pp., Natl. Oceanogr. Data Cent., Silver Spring, Md.
- Cravatte, S., J. Picaut, and G. Eldin (2003), Second and first baroclinic Kelvin modes in the equatorial Pacific at intraseasonal timescales, *J. Geophys. Res.*, **108**(C8), 3266, doi:10.1029/2002JC001511.
- Crépon, M., and C. Richez (1982), Transient upwelling generated by two-dimensional atmospheric forcing and variability in the coastline, *J. Phys. Oceanogr.*, **12**, 1437–1457, doi:10.1175/1520-0485(1982)012<1437:TUGBTD>2.0.CO;2.
- da Silva, A. M., C. C. Young-Molling, and S. Levitus (Eds.) (1994) *Atlas of Surface Marine Data 1994*, vol. 1, *Algorithms and Procedures*, NOAA Atlas NESDIS, vol. 6, 83 pp., NOAA, Silver Spring, Md.
- Dewitte, B., S. Purca, S. Illig, L. Renault, and B. S. Giese (2008), Low frequency modulation of intraseasonal equatorial Kelvin wave activity in the Pacific from SODA: 1958–2001, *J. Clim.*, **21**, 6060–6069, doi:10.1175/2008JCLI2277.1.
- Ducet, N., P. Y. Le Traon, and G. Reverdin (2000), Global high-resolution mapping of ocean circulation from TOPEX/Poseidon and ERS-1 and -2, *J. Geophys. Res.*, **105**, 19,477–19,498, doi:10.1029/2000JC900063.
- Garreaud, R. D., and R. C. Muñoz (2005), The low-level jet off the west coast of subtropical South America: Structure and variability, *Mon. Weather Rev.*, **133**, 2246–2261, doi:10.1175/MWR2972.1.
- Kessler, W. (2006), The circulation of the eastern tropical Pacific: A review, *Prog. Oceanogr.*, **69**, 181–217, doi:10.1016/j.pcean.2006.03.009.
- Large, W. G., J. C. McWilliams, and S. C. Doney (1994), Oceanic vertical mixing: A review and a model with a nonlocal boundary layer parameterization, *Rev. Geophys.*, **32**, 363–403, doi:10.1029/94RG01872.
- Lengaigne, M., J.-P. Boulanger, C. Menkes, S. Masson, P. Delecluse, and G. Madec (2002), Ocean response to the March 1997 westerly wind event, *J. Geophys. Res.*, **107**(C12), 8015, doi:10.1029/2001JC000841.
- Lett, C., P. Penven, P. Ayón, and P. Fréon (2007), Enrichment, concentration and retention processes in relation to anchovy (*Engraulis ringens*) eggs and larvae distributions in the Northern Humboldt Upwelling Ecosystem, *J. Mar. Syst.*, **64**, 189–200, doi:10.1016/j.jmarsys.2006.03.012.
- Lukas, R. (1986), The termination of the equatorial undercurrent in the eastern Pacific, *Prog. Oceanogr.*, **16**, 63–90, doi:10.1016/0079-6611(86)90007-8.
- Madden, R. A., and P. R. Julian (1971), Detection of a 40–50 day oscillation in the zonal wind field of the tropical Pacific, *J. Atmos. Sci.*, **28**, 702–708, doi:10.1175/1520-0469(1971)028<0702:DOADOI>2.0.CO;2.
- Madden, R. A., and P. R. Julian (1972), Description of global-scale circulation cells in the tropics with a 40–50 day period, *J. Atmos. Sci.*, **29**, 1109–1123, doi:10.1175/1520-0469(1972)029<1109:DOGCC>2.0.CO;2.
- Madec, G., P. Delecluse, M. Imbard, and C. Levy (1998), OPA 8.1 ocean general circulation model reference manual, *Notes IPSL* **11**, 91 pp., Univ. Pierre et Marie Curie, Paris.
- Marchesiello, P., J. C. McWilliams, and A. Shchepetkin (2001), Open boundary conditions for long-term integration of regional oceanic models, *Ocean Modell.*, **3**, 1–20, doi:10.1016/S1463-5003(00)00013-5.
- Marchesiello, P., J. C. McWilliams, and A. Shchepetkin (2003), Equilibrium structure and dynamics of the California Current System, *J. Phys. Oceanogr.*, **33**, 753–783, doi:10.1175/1520-0485(2003)33<753:ESADOT>2.0.CO;2.
- Montes, I., F. Colas, X. Capet, and W. Schneider (2010), On the pathways of the equatorial subsurface currents in the eastern equatorial Pacific and their contributions to the Peru–Chile Undercurrent, *J. Geophys. Res.*, **115**, C09003, doi:10.1029/2009JC005710.
- Penven, P., V. Echevin, J. Pasapera, F. Colas, and J. Tam (2005), Average circulation, seasonal cycle, and mesoscale dynamics of the Peru Current System: A modeling approach, *J. Geophys. Res.*, **110**, C10021, doi:10.1029/2005JC002945.
- Penven, P., P. Marchesiello, L. Debreu, and J. Lefèvre (2008), Software tools for pre- and post-processing of oceanic regional simulations, *Environ. Model. Softw.*, **23**, 660–662, doi:10.1016/j.envsoft.2007.07.004.
- Ramos, M., O. Pizarro, L. Bravo, and B. Dewitte (2006), Seasonal variability of the permanent thermocline off northern Chile, *Geophys. Res. Lett.*, **33**, L09608, doi:10.1029/2006GL025882.
- Renault, L., B. Dewitte, M. Falvey, R. Garreaud, V. Echevin, and F. Bonjean (2009), Impact of atmospheric coastal jet off central Chile on SST from satellite observations (2000–2007), *J. Geophys. Res.*, **C08006**, doi:10.1029/2008JC005083.
- Saunders, P. M., A. C. Coward, and B. A. de Cuevas (1999), Circulation of the Pacific Ocean seen in a global ocean model (OCCAM), *J. Geophys. Res.*, **104**, 18,281–18,299, doi:10.1029/1999JC900091.
- Shchepetkin, A. F., and J. C. McWilliams (1998), Quasi-monotone advection schemes based on explicit locally adaptive dissipation, *Mon. Weather Rev.*, **126**, 1541–1580.
- Shchepetkin, A. F., and J. C. McWilliams (2005), The regional oceanic modeling system (ROMS): A split-explicit, free-surface, topography following- coordinate oceanic model, *Ocean Modell.*, **9**, 347–404, doi:10.1016/j.ocemod.2004.08.002.
- Shchepetkin, A. F., and J. C. McWilliams (2009), Correction and commentary for “Ocean forecasting in terrain-following coordinates: Formulation and skill assessment of the regional ocean modeling system” by Haidvogel et al., *J. Comput. Phys.*, **228**, 8985–9000, doi:10.1016/j.jcp.2009.09.002.
- Silva, N., and S. Neshyba (1979), On the southernmost extension of the Peru–Chile Undercurrent, *Deep Sea Res. Part A*, **26**, 1387–1393.
- Smith, W. H. F., and D. T. Sandwell (1997), Global seafloor topography from satellite altimetry and ship depth soundings, *Science*, **277**, 1957–1962.
- Strub, P., J. Mesias, and C. James (1995), Altimeter observations of the Peru–Chile countercurrent, *Geophys. Res. Lett.*, **22**, 211–214, doi:10.1029/94GL02807.
- Strub, P. T., J. M. Mesias, V. Montecino, J. Rutllant, and S. Salinas (1998), Coastal ocean circulation off western South America, in *The Sea*, vol. 11, edited by A. R. Robinson and K. H. Brink, pp. 273–313, John Wiley, New York.
- Uppala, S. M., et al. (2005), The ERA-40 re-analysis, *Q. J. R. Meteorol. Soc.*, **131**, 2961–3012, doi:10.1256/qj.04.176.

A. Chaigneau and V. Echevin, LOCEAN/IRD/IPSL/UPMC, Case 100, 4 Place Jussieu, F-75252 Paris CEDEX 05, France. (vincent.echevin@locean-ipsl.upmc.fr)

F. Colas, CESR, IGPP, UCLA, 405 Charles E. Young Dr., Los Angeles, CA 90095, USA.

P. Penven, UMR 5563, LPO/IRD/UBO, BP 70, F-29280 Plouzané, France.